Aerospace Science and Technology 117 (2021) 106980

Contents lists available at ScienceDirect

Aerospace Science and Technology

www.elsevier.com/locate/aescte

A 3D implicit structured multi-block grid finite volume method for computational structural dynamics

Li Ma [a], George N. Barakos [b,*], Qijun Zhao [a]

[a] National Key Laboratory of Rotorcraft Aeromechanic, Nanjing University of Aeronautics and Astronautics, Nanjing 210016, China
[b] CFD Laboratory, School of Engineering, University of Glasgow, Glasgow, G12 8QQ, Scotland, UK

ARTICLE INFO

Article history:
Received 26 January 2021
Received in revised form 28 June 2021
Accepted 13 July 2021
Available online 22 July 2021
Communicated by Saravanos Dimitris

Keywords:
Finite volume method
Computational structural dynamics
Multi-block grids
Matrix-free dual time-stepping
Dynamic response
Airfoil

ABSTRACT

This work aims to develop a FVM-based structural solver that can seamlessly be integrated with Computational Fluid Dynamics (CFD) solvers for fluid-structure interaction (FSI) problems. For flexibility in gridding and efficient computation, hexahedral multi-block grids are adopted which are locally structured, but globally unstructured. Besides, ghost cells are introduced to solve the partial derivatives and displacements at the boundaries of the computational domain. Time-accurate solutions are obtained by employing a matrix-free, dual time stepping approach, and the implicit residual value smoothing method is used to increase the convergence rate. Stresses are evaluated using Green's theorem based on the gradients of the displacement of the cells. The proposed method is applied to static and dynamic response of 3D cantilevers. Results are found to agree well with analytical solutions, and the amplitude error of the dynamic response is less than 1.5%. Besides, resonance and beating phenomena were clearly observed and compared to Finite Element approaches in accuracy and efficiency. Finally, the dynamic response of a cantilever beam with NACA0012 airfoil is analyzed preliminarily.

0. Introduction

Fluid-structure interaction (FSI) is one of the most important problems in aeronautical engineering design and analysis. There are many applications of the FSI in body vibration of hypersonic inlets [1], aeroelastic deformation of wings and rotors [2], and missile design [3]. The main components of the FSI framework include a CFD solver, a CSD solver, and a grid deformation method [4]. With the development of grid deformation technology [5][6], more and more attention has been paid to the CFD/CSD coupling method. The finite volume method (FVM) is usually used to solve the fluid term equation, and the finite element method (FEM) is used to solve the structure mechanics. Unlike the FEM that only satisfies the relevant conservation principles and equilibrium of forces in a global sense, the FVM is conservative from the whole domain scale to the element or control volume level. To emphasize the different control volumes used by the finite element and finite volume methods the domain, in Fig. 1, is split with the left-hand portion representing the finite element method and the right-hand portion representing the finite volume method. Essentially, the finite element method integrates the equilibrium or conservation equations over these control volumes and uses numerical integration (i.e. Gauss quadrature) techniques to approximate the volume integrals in three dimensions or area integrals in two dimensions. The essence of the finite volume discretization technique is to integrate the equilibrium or conservation equations over control volumes and then use the divergence theorem to transform the volume integrals to surface integrals (in three dimensions and area integrals into line integrals in two dimensions). The quantities within the surface integrals are then approximated at integration points located within the grid elements on the surface of the control volumes. A continuum field which undergoes motion is governed by the Cauchy's equation which is valid for structural and fluid dynamics.

Their different attributes, applications and development directions have led to software implementations of FEM and FVM for CFD and CSD being different in almost every aspect, which leads to compatibility issues between CFD and CSD software. As a result, the progress in finding a unified FVM solver to simulate the multi-physical problems of fluid-structure interaction is hindered. Unless the fluid-structure coupling problem studied is unidirectional or only needs a small amount of information exchange, the data transfer from

* Corresponding author.
E-mail address: george.barakos@glasgow.ac.uk (G.N. Barakos).

https://doi.org/10.1016/j.ast.2021.106980

Nomenclature

Notations

ρ	density
$\boldsymbol{V}$	velocity vector
$\boldsymbol{U}$	displacement vector
$\boldsymbol{f}$	body force
$\boldsymbol{\sigma}$	stress tensor
$\boldsymbol{\varepsilon}$	strain tensor
E	Young's modulus
ν	Poisson's ratio
$\boldsymbol{I}$	the unit tensor
μ and λ	Lamé's coefficients
v_p	control volume
s	surface of volume
$\Delta\tau$	pseudo time step
Δt	real time step
$\boldsymbol{M}$	bending moment
I_z	Area moment of inertia

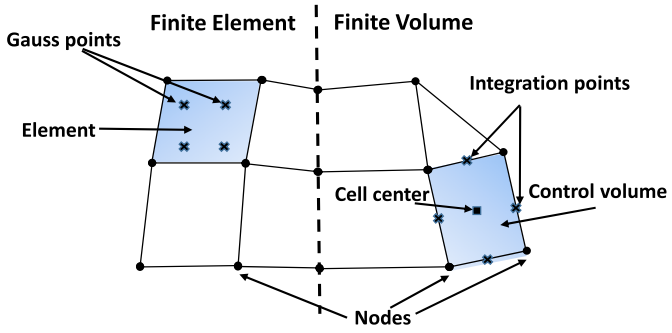

Fig. 1. Grid element and control volumes for both finite elements and finite volume.

one grid to another may lead to poor convergence and energy losses. FEM is generally considered to be more accurate for self-joint problems, which are typical of CSD. However, the essential difference between FEM and FVM in the numerical discretization of second-order partial differential equations is rather limited, and for some cases, the two methods are equivalent [7][8]. The fact that the form of equations of Stokes flows is similar to the form of equations of isotropic incompressible linear elastic solids has motivated many researchers to implement CFD methods, developed for the solution of incompressible fluid flows, for modelling displacement in solids.

Over the last thirty years, the FV method has been applied to an extensive range of problems in CSD, appearing in several distinct forms: "Standard" FVM approaches, Matrix-free approaches and other approaches. The "standard" FVM approaches [9–21] employ implicit solution methodologies, where a system of linear algebraic equations is solved via iterative or direct methods. These implicit methods require the formation and inversion of a sparse matrix, where the surface force term within the momentum equation is discretized implicitly in terms of the primitive variables. In contrast, the matrix-free approaches evaluate the surface force term using the older time-step values of the primitive variable, avoiding the construction of a linear matrix system [22]. Given the distinction in solution methodology, matrix-free methods merit separate consideration; however, these approaches typically adopt vertex-centred, and in some cases, cell-centred, spatial discretizations and could equally be considered under those headings. Lv et al. [23] and Xia et al. [24][25] developed a vertex-based finite volume approach with non-overlapping control volumes that do not use shape functions. Sabbagh-Yazdi and co-workers [26–29] developed a similar vertex-centre d approach, which has been used to analyze 2-D elastic thermo-elastic problems including crack propagation in concrete; they followed the Galerkin finite volume method, and implemented in an in-house tool called NASIR (Numerical Analyzer for Scientific and Industrial Requirements). The Galerkin finite volume method here uses a piecewise constant distribution of the primary variables. Similar approaches were developed by Chen and Yu [30] for impact analysis of thin plates, by Zhu et al. [31] for stress wave propagation, by Tsui et al. [32] for fluid-solid interactions, and by Suliman et al. [33] for bending beams. Alagappan et al. [34][35] developed a novel staggered grid finite volume technique for wave propagation problems in viscoelastic solids, where the displacement is calculated at alternating nodes to the stress. Hejranfar and Azampour [36] compared performance of cell-centred and cell-vertex approaches, and the results indicated that the two approaches are equivalent in terms of accuracy and convergence rate on regular grids. Selim et al. [37] developed a cell-centred matrix-free dual time-stepping method for fluid-solid interaction problems, where the solid spatial discretization closely resembles the standard Demirdzic and Muzaferija method. However, the results are relatively simple, and only the free end response of cantilever under steady load excitation is compared with the results of FEM. So far, no detailed grid independence analysis, convergence and efficiency analysis have been carried out for 3D dynamics. It is not clear whether the matrix-free finite volume method has the same accuracy in simulating forced vibration under higher harmonic loads like FEM. Besides, in the development of the matrix-free finite volume method, the structured grid has not been adopted to calculate and analyze the CSD problems. In the case of the same number of grid points, the memory and CPU time requirement for unstructured grids may be more expensive than that for structured grids [38] (more prominent in the case of three-dimensional). Besides, when an unstructured grid is used for discretization, the precision depends to the isotropy of the grid distribution. The structured grid can be easily indexed, and the corresponding memory is reduced. When the computational domain is relatively simple, a single-domain body-fitted structure grid can be used. Multi-block structured methods [39,40] will be adopted here as the complexity of the research problem increases.

In this paper, the hexahedral structural grids are introduced to a matrix-free finite volume method of cell-centred scheme for 3D linear elasticity problems. Ghost cells are applied to compute the partial derivatives and displacements at the boundary of the computational domain. Multi-block grids are adopted to obtain flexibility in gridding as well as efficient computation. Time-accurate solutions are obtained by employing a matrix-free dual time stepping approach, which is solved using the five-stage Runge-Kutta integration method and can reduce computational efforts and storage requirements. The physical time is discretized using an implicit second-order accurate backward

differencing scheme, and the implicit residual value smoothing method is used to increase the convergence rate. The proposed method is applied to static and dynamic response of 3D cantilevers. Results agree well with analytical solutions, and the amplitude error of dynamic response is less than 1.5%. This is a first step towards the development of a finite volume FSI methods for aeroelastic studies.

1. Numerical methodology

1.1. Governing equations

The governing equations for a moving structure can be written as,

$$\frac{\partial(\rho \boldsymbol{V})}{\partial t} - \nabla \cdot \boldsymbol{\sigma} + \rho C \frac{\partial \boldsymbol{U}}{\partial t} = \rho \boldsymbol{f} \tag{1}$$

where $\boldsymbol{V}$ is the velocity vector, $\boldsymbol{U} = \begin{bmatrix} u \\ v \\ w \end{bmatrix}$ is the displacement vector, ρ is the density, C is the damping coefficient, $\boldsymbol{f}$ is the body force per unit mass, and $\boldsymbol{\sigma} = \begin{bmatrix} \sigma_{xx} \tau_{xy} \tau_{xz} \\ \tau_{yx} \sigma_{yy} \tau_{yz} \\ \tau_{zx} \tau_{zy} \sigma_{zz} \end{bmatrix}$ is the stress tensor.

1.2. Constitutive relation

The generalized form of Hook's law provides the following stress-strain relationship for isotropic homogeneous material undergoing small strains:

$$\boldsymbol{\sigma} = 2\mu \boldsymbol{\varepsilon} + \lambda \nabla \bullet \boldsymbol{U} \boldsymbol{I} \tag{2}$$

Where, $\boldsymbol{I}$ is the unit tensor and μ and λ are Lamé's coefficients, relating to Young's modulus of elasticity E, and the Poisson's ratio ν as:

$$\mu = \frac{E}{2(1+\nu)}, \qquad \lambda = \begin{cases} \frac{\nu E}{(1+\nu)(1-\nu)} & \text{Plane stress} \\ \frac{\nu E}{(1+\nu)(1-2\nu)} & \text{Plane strain and 3D} \end{cases} \tag{3}$$

The strain tensor $\boldsymbol{\varepsilon}$ is defined in terms of the displacement vector $\boldsymbol{U}$ as follows:

$$\boldsymbol{\varepsilon} = \frac{1}{2}\left[\nabla \boldsymbol{U} + (\nabla \boldsymbol{U})^T\right] \tag{4}$$

By substituting Eq. (2) into Eq. (1) and writing the stress tensor in terms of the gradient of the displacement $\nabla \boldsymbol{U}$, Eq. (1) can be written as:

$$\frac{\partial(\rho \boldsymbol{V})}{\partial t} - \nabla \bullet \left[\mu \nabla \boldsymbol{U} + \mu (\nabla \boldsymbol{U})^T + \lambda \nabla \bullet \boldsymbol{U} \boldsymbol{I}\right] + \rho C \frac{\partial \boldsymbol{U}}{\partial t} = \rho \boldsymbol{f} \tag{5}$$

1.3. Discretization method

Integrating Eq. (5) over a control volume v_p with boundary ∂v_p as the control surface and applying the Gauss' theorem, and Eq. (5) can be discretizated as:

$$\int_{v_p} \frac{\partial(\rho \boldsymbol{V})}{\partial t} dv_p - \oint_{\partial v_p} ds \cdot \left[\mu \nabla \boldsymbol{U} + \mu (\nabla \boldsymbol{U})^T + \lambda \nabla \bullet \boldsymbol{U} \boldsymbol{I}\right] + \int_{v_p} \rho C \frac{\partial \boldsymbol{U}}{\partial t} dv_p = \int_{v_p} \rho \boldsymbol{f} dv_p \tag{6}$$

1.4. Spatial discretization

In CSD, similar to CFD, FVM has been classified into two approaches, cell centred and cell-vertex. For the cell-centred method (see Fig. 2 (a)), the control volumes are the actual grid elements. The cell-vertex method represented in Fig. 2 (b) uses control volumes are generated by effected centres of the grid elements to the mid points of their faces. This creates subcontrol volumes that contribute to the overall control volume of a node. Combining all the subcontrol volumes from grid elements related to a node, gives polyhedral-type cells that surround each node representing the vertices of the grid elements. The cell-centred FV approach has been the most common method in CFD and it can efficiently support most of the CFD codes for the simulation of fluid flows in an accurate and efficient manner.

The governing equation (5) is discretized on a hexahedral element, as shown in Fig. 3. O is the centre of the cell, and for cell-centred formulation, the calculated variables are stored in O. The six surfaces of the element constitute the corresponding control volume surface, and are used to calculate the strain, stress and external force.

The continuous surface integrals in Eq. (6) are split into the sum of integrals over the cell faces

$$\oint_{\partial v_p} ds \cdot \left[\mu \nabla \boldsymbol{U} + \mu (\nabla \boldsymbol{U})^T + \lambda \nabla \bullet \boldsymbol{U} \boldsymbol{I}\right] = \sum_{faces} s \cdot \left[\mu \nabla \boldsymbol{U} + \mu (\nabla \boldsymbol{U})^T + \lambda \nabla \bullet \boldsymbol{U} \boldsymbol{I}\right] \tag{7}$$

where s is the face area vector.

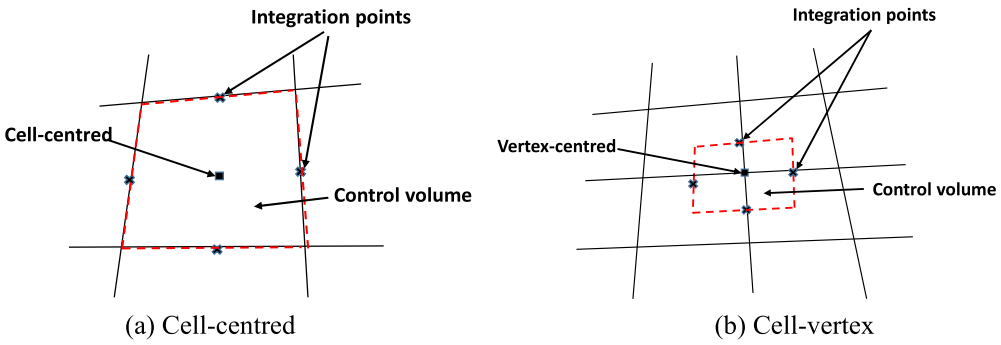

Fig. 2. Different finite volume procedures.

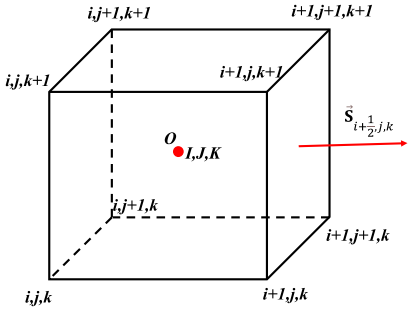

Fig. 3. Schematic of a 3D hexahedral grid element.

1.5. Dual time-stepping scheme

The temporal derivative is calculated using properties at $n+1$, n, and $n-1$ time levels

$$\int_v \frac{\partial(\rho \boldsymbol{V})}{\partial t} dv = \rho v_p \left[\frac{3\boldsymbol{V}^{n+1} - 4\boldsymbol{V}^n + \boldsymbol{V}^{n-1}}{2\Delta t}\right] \tag{8}$$

where $\boldsymbol{V}^{n+1} = \boldsymbol{V}(t+\Delta t)$, $\boldsymbol{V}^n = \boldsymbol{V}(t)$ and $V^{n-1} = \boldsymbol{V}(t-\Delta t)$.

By assembling all terms and performing the integrations, we obtain:

$$\rho v_p \left[\frac{3V^{n+1} - 4V^n + \boldsymbol{V}^{n-1}}{2\Delta t}\right] - \sum_{faces} s \cdot \left[\mu \nabla \boldsymbol{U}^n + \mu(\nabla \boldsymbol{U}^n)^T + \lambda \nabla \bullet \boldsymbol{U}^n \boldsymbol{I}\right] + \rho v_p \left(C\boldsymbol{V}^n - \boldsymbol{F}\right) = 0 \tag{9}$$

Following the standard Dual Time-Stepping based finite volume method [37], the displacement gradients are evaluated numerically at the cell centre. Therefore, according to Gauss's divergence theorem, the displacement gradients are given by:

$$\nabla \boldsymbol{U}_{cell} = \left[\sum_{faces} \vec{n} \bullet \boldsymbol{U}_{face}\right] / v_p \tag{10}$$

where $\vec{n}$ is the normal vector. The ∇U and U of the cell surface is obtained by averaging the adjacent cell centre, as shown in Fig. 4:

$$\begin{aligned} \nabla \boldsymbol{U}_{i+1/2,j} &= \frac{1}{2}\left(\nabla \boldsymbol{U}_{i,j} + \nabla \boldsymbol{U}_{i+1,j}\right) \\ \boldsymbol{U}_{i+1/2,j} &= \frac{1}{2}\left(\boldsymbol{U}_{i,j} + \boldsymbol{U}_{i+1,j}\right) \end{aligned} \tag{11}$$

To achieve a matrix-free operation and to use a larger time step size, a dual time-stepping scheme is adopted by adding a pseudo time derivative term to the left-hand side of Eq. (9). This dual-time-stepping procedure is independent of the spatial discretization approach employed, i.e. in finite volume or finite element methods. After adding the pseudo term into Eq. (9), we have:

$$\frac{d\boldsymbol{V}^{n+1}}{d\tau} = \frac{1}{\rho v_p} \sum_{faces} s \cdot \left[\mu \nabla \boldsymbol{U}^n + \mu(\nabla \boldsymbol{U}^n)^T + \lambda \nabla \bullet \boldsymbol{U}^n \boldsymbol{I}\right] - \left[\frac{3\boldsymbol{V}^{n+1} - 4\boldsymbol{V}^n + \boldsymbol{V}^{n-1}}{2\Delta t}\right] - \left(C\boldsymbol{V}^n - \boldsymbol{F}\right) = Res\left(\boldsymbol{U}^{n+1}\right) \tag{12}$$

Then, the solution is sought by marching in τ to a converged state. A five-stage Runge-Kutta scheme is used to integrate Eq. (12) for stability and fast convergence. According to this method:

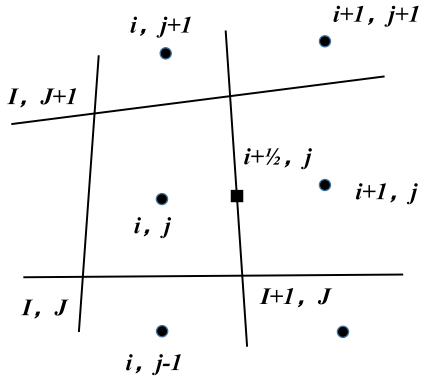

Fig. 4. Schematic diagram of the displacement gradient calculation on a cell surface.

$$
\begin{aligned}
&\boldsymbol{V}^{(0)} = \boldsymbol{V}^{(n,m)},\\
&\boldsymbol{V}^{(1)} = \boldsymbol{V}^{(0)} + \alpha_1 \Delta\tau \boldsymbol{Res}^{(0)},\\
&\boldsymbol{V}^{(2)} = \boldsymbol{V}^{(0)} + \alpha_2 \Delta\tau \boldsymbol{Res}^{(1)},\\
&\boldsymbol{V}^{(3)} = \boldsymbol{V}^{(0)} + \alpha_3 \Delta\tau \boldsymbol{Res}^{(2)},\\
&\boldsymbol{V}^{(4)} = \boldsymbol{V}^{(0)} + \alpha_4 \Delta\tau \boldsymbol{Res}^{(3)},\\
&\boldsymbol{V}^{(5)} = \boldsymbol{V}^{(0)} + \alpha_5 \Delta\tau \boldsymbol{Res}^{(4)},\\
&\boldsymbol{V}^{(n,m+1)} = \boldsymbol{V}^{(5)},
\end{aligned}
\tag{13}
$$

where the superscript m denotes the pseudo time level and the coefficients for the five-stage Runge-Kutta time integration are taken as $\alpha_1 = 0.25$, $\alpha_2 = 0.167$, $\alpha_3 = 0.375$, $\alpha_4 = 0.500$, $\alpha_5 = 1.000$.

After the velocity is obtained, the displacement is calculated using the average of V^n and V^{n+1} as

$$\boldsymbol{U}^{t+1} = \boldsymbol{U}^t + \frac{\Delta t}{2}\left(\boldsymbol{V}^{t+1} + \boldsymbol{V}^t\right) \tag{14}$$

The residuals are given by the following:

$$RES_{total} = \sqrt{\sum_{cells}(\boldsymbol{U}^{n+1} - \boldsymbol{U}^n)^2}/N_{cell} \tag{15}$$

The dual-time stepping procedure is a conditionally stable scheme since it is explicit in pseudo-time, meaning a limit exists on the pseudo-time step size $\Delta\tau$. However, the procedure is implicit in real-time, and the scheme is stable for any choice of the real-time step size Δt. To ensure stability, the pseudo time step must be less than the critical pseudo time step, which is defined by the following expression:0

$$\Delta\tau = \mathrm{CFL} \bullet \frac{L}{\sqrt{\frac{\kappa}{\rho}} + \sqrt{\frac{\mu}{\rho}}}. \tag{16}$$

Here L is the effective length scale of the grid spacing, and K is the bulk modulus which is defined as

$$\kappa = \frac{E}{3(1-2\nu)} \tag{17}$$

To improve the convergence rate, residual smoothing [15] is adopted, which only destroys time accuracy in pseudo time without affecting the accuracy in real time. The idea behind this is to replace the residual at one vertex with a smoothed or weighted average of the residuals at the neighbouring vertices. The averaged residuals are calculated implicitly in order to increase the local pseudo time step size, thus increasing the convergence rate. The smoothing equation for a vertex k can be expressed as:

$$
\begin{aligned}
&-\varepsilon^I \boldsymbol{R}^*_{I-1,J,K} + (1+2\varepsilon^I)\boldsymbol{R}^*_{I,J.K} - \varepsilon^I \boldsymbol{R}^*_{I+1,J.K} = \boldsymbol{R}_{I,J,K}\\
&-\varepsilon^J \boldsymbol{R}^{**}_{I,J-1,K} + (1+2\varepsilon^J)\boldsymbol{R}^{**}_{I,J,K} - \varepsilon^J \boldsymbol{R}^{**}_{I,J+1,K} = \boldsymbol{R}^*_{I,J,K}\\
&-\varepsilon^K \boldsymbol{R}^{***}_{I,J,K-1} + (1+2\varepsilon^J)\boldsymbol{R}^{***}_{I,J,K} - \varepsilon^J \boldsymbol{R}^{***}_{I,J,K+1} = \boldsymbol{R}^{**}_{I,J,K}
\end{aligned}
\tag{18}
$$

where $\boldsymbol{R}^*, \boldsymbol{R}^{**}, \boldsymbol{R}^{***}$ represent the residual values of I, J, K directions after smoothing, and $\varepsilon^I, \varepsilon^J, \varepsilon^K$ represents the residual smoothing coefficients of the three calculated coordinates, which can be defined as

$$\varepsilon = \max\left\{\frac{1}{4}[(\frac{\Delta\tau}{\Delta\tau^*})^2 - 1], 0\right\} \tag{19}$$

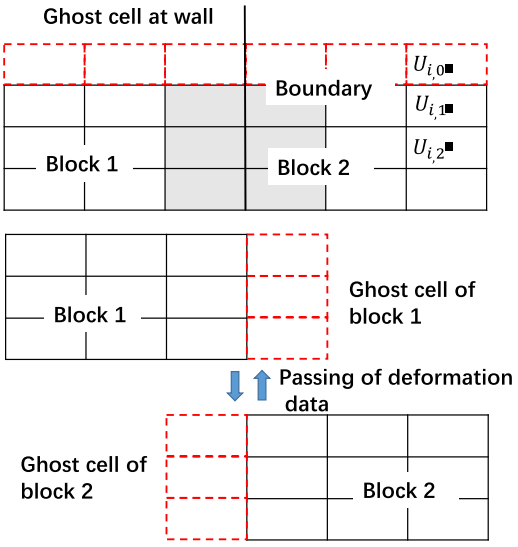

Fig. 5. Boundary condition sketch of multi-block and ghost grid.

Here, $\Delta\tau^*$ is the maximum $\Delta\tau$ of the basic scheme. The implicit operator in equation (18) is similar to the second-order central difference, so it is also called the central scheme residual smoothing. Generally, the pursuit method of the tridiagonal matrix is used to solve equation (18).

1.6. Boundary conditions and multi-block grids

Traditionally, cell-centred FVM incorporates boundary conditions directly into the discretized equations for the control volumes adjacent to boundaries [37][41][42][44]. However, an implicit calculation of tangential gradients along near-boundary faces becomes complicated. In this work, ghost cells [43] are introduced to deal with boundary conditions. It should be emphasized that not only displacement and gradient boundary conditions, but also velocity boundary conditions on fixed end must be introduced in matrix-free FVM to solve solid dynamic problems, otherwise numerical oscillation was occurred.

(A) For fixed boundary conditions, the following conditions are applied:

(a) $\boldsymbol{U}_{i,0} = -\boldsymbol{U}_{i,1}$

(b) $\boldsymbol{V}_{fixed\ end} = 0$

(c) $\nabla\boldsymbol{U}_{i,0} = \nabla\boldsymbol{U}_{i,1}$

(B) For traction boundary conditions, the following conditions are applied:

(a) $\boldsymbol{U}_{i,0} = 3\boldsymbol{U}_{i,1} - 2\boldsymbol{U}_{I,2}$

(b) $\nabla\boldsymbol{U}_{i,0} = -\nabla\boldsymbol{U}_{i,1}$

(C) For the boundary between adjacent grid blocks (see Fig. 5), the $U_{i,j}$ and $\nabla U_{i,j}$ on the ghost grid are directly obtained from the internal points of the connected grid blocks.

Finally, Eq. (11) is used to solve the displacement and gradient on the cell faces for the whole calculation domain. The ghost cells make the spatial discretization easier.

1.7. Grid deformation

The grid deformation of FVM is realized by node coordinates plus node displacement. The value of the cell node is obtained from the cell centre of the surrounding eight cells, and the calculation formula is as follows:

$$\boldsymbol{U}_{nodes} = \frac{\sum_{i=1}^{8}\left(\boldsymbol{U}_{i,center} \bullet v_{p_i}\right)}{\sum_{i=1}^{8} v_{p_i}} \tag{20}$$

2. Numerical results and analyses

2.1. Verification of grid independence in 3D dynamics

A standard problem in structural mechanics is that of a fixed-free cantilever supporting a distributed force load on its upper surface [24][37][24][44]. Table 1 lists the material and geometric specifications of the cantilever beam.

Table 1
Cantilever dimensions and material properties.

Dimension	Value	Property	Value
Length, L	2 m	Density	1000 Kg m^{-3}
Width, d	0.2 m	Young's modulus	15.293 MPa
Height, b	0.2 m	Poisson's	0.3

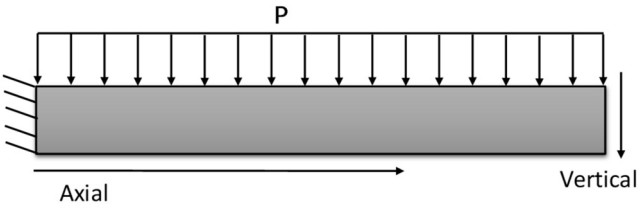

Fig. 6. Schematic of the cantilevered beam under a distributed pressure load.

Table 2
Grid size and convergence steps of the 3D cantilevered beam.

Grid	Cells	Nodes	CFL_{max}	Convergence steps to 10^{-8}
No.1	$5 \times 5 \times 20$	756	8	21
No.2	$5 \times 5 \times 50$	1836	20	28
No.3	$5 \times 10 \times 50$	3366	8	76
No.4	$10 \times 10 \times 50$	6171	10	79
No.5	$10 \times 10 \times 100$	12221	18	87
No.6	$20 \times 20 \times 200$	88641	20	288

The natural frequency of a uniform cantilever beam is given by the following formula:

$$f = \frac{3.516}{2\pi L^2}\left(\frac{EI_z}{\rho bd}\right)^{1/2} \tag{21}$$

where I is the moment of inertia. According to Eq. (21), the basic natural frequency of the cantilever beam is 1 Hz, and the vibration period is 1 s. A uniform distributed pressure is added as shown in Fig. 6, and the applied uniform pressure, P, value was set to 510.0 Pa.

To compare with the finite element method, the commercial software ANSYS^{TM} is applied for numerical simulation. A 3D formulation is used with U_x, U_y, U_z degrees of freedom and transient analysis is applied to simulate the dynamic response. The equation is solved by preconditioned conjugate gradient (PCG), and Newton-Raphson is used to improve convergence.

Firstly, the dynamic (undamped) response was simulated. Based on the analytical solution and the calculated natural frequency, the maximum dynamic deflection at the free end of the beam is 0.2 m and takes place at $t = 0.5$ seconds. The physical time step was set to 1×10^{-3} seconds, and the order of convergence is 10^{-8}. For all cases, the load was suddenly applied at $t = 0$ seconds and kept till the end of the simulation. Moreover, the structure was assumed to be initially stationary.

The details of the calculations shown in Table 2. As grids become finer, the iterations steps also increase, and for more orthogonal grids, the CFL can reach a larger value, which effectively improves the convergence speed.

Fig. 7 and Table 3 show the dynamic tip response of the cantilevered beam with different grid sizes. There is about more than 10% errors in phase and amplitude predictions on grids $1(5 \times 5 \times 20)$ and $2(5 \times 5 \times 50)$. With the increase of grid cells, the accuracy of amplitude and phase results improved rapidly. The maximum amplitude for grid $6(20 \times 20 \times 200)$ is 0.1974 m, and the error is reduced to -1.290%, while the error of the FEM method is 2.150%. After 2.5 periods of vibration, the phase error is 0.640%, and the error is defined as:

$$Error = \frac{U_{cal} - U_{Analytic}}{U_{Analytic}} \times 100\% \tag{22}$$

Compared with the analytical solution, the amplitude is under predicted by the FVM solution, and over predicted by the FEM. The percentages of the errors in the z displacement are listed in Table 3. A percentage error of 1.845% is found with grid 4. Thus grid 4, 5, 6 are deemed to fine enough, and are chosen for further analysis. Selim [44] represents a 2% amplitude error and a 1.6% frequency shift with 20,000 unstructured grid points.

The iteration steps converging to 10^{-8} for each pseudo time step and CFL_{max} are shown in Table 2. As grids become refined, the iterations also increased, and CFL could reach get a larger value for cube grids. The residuals of the six grids are shown in Fig. 8. The convergence of grid 6 is obviously lower than that of the other five grids. Besides, since grid 6 is the most refined and the matrix-free FVM integrates on faces, the time required for each iteration increases.

Both FVM and FEM have been performed using i7-4790 processors, using single thread computing. The single processor CPU time for each grid is presented in Table 3. Even if the grid size is small, the FEM method maintains high accuracy, and the solution time is proportional to the number mesh cells. The matrix-free FVM has higher computational efficiency than FEM. This is mainly due to that every real time step of FEM needs to solve large-scale linear equations, and the matrix-free FVM solved the displacement response by pseudo time step. However, the solution time of FVM is not proportional to the number of grid points, because the convergence of the dual time step iteration is also related to the CFL number. The results show that the efficiency and accuracy of FVM could be higher than

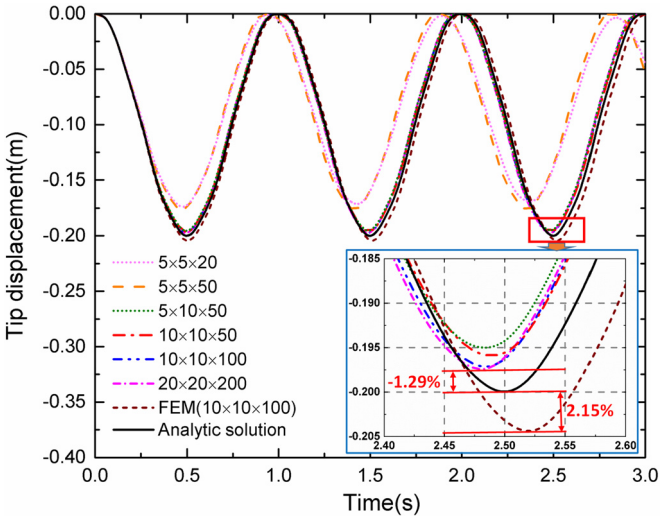

Fig. 7. Dynamic response of the cantilevered under uniform distributed pressure with different grid sizes.

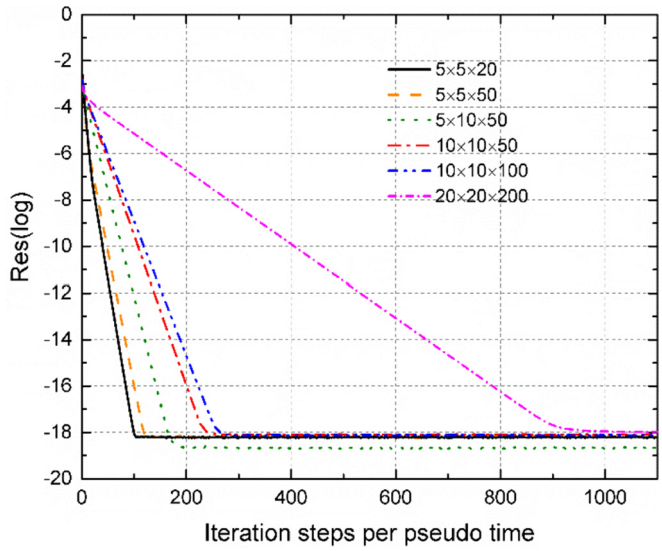

Fig. 8. Convergence plots with different grid sizes.

Table 3
Comparison of CPU time and accuracy of FVM and FEM.

Grid	Total time of FVM (s)	Total time of FEM (s)	Error of FVM (%)	Error of FEM (%)
5 × 5 × 20	50.1	956	−13.045	2.21
5 × 5 × 50	138	2142	−11.93	2.20
5 × 10 × 50	570	4848	−2.29	2.16
10 × 10 × 50	1110	10116	−1.84	2.15
10 × 10 × 100	2670	18630	−1.43	2.15
20 × 20 × 200	44924	157215	−1.29	2.15

FEM on a refined grid. It can be observed that grid 5 shows high efficiency while ensuring good calculation accuracy, and will be used in the following calculations.

The displacement distribution with the velocity boundary condition is shown in Fig. 9, and it can be observed that there were violent numerical oscillations at the fixed end of the cantilever when no velocity boundary condition was applied. If the mesh is refined enough, this may lead to negative cell volumes after grid deformation, calculation failure, and large errors in the root stress analysis. The oscillations gradually weaken along the axial direction.

Fig. 10 shows the stress distribution of fixed end at 0.5 s. The distributed force causes a moment in the lagging direction at the fixed end, leading to σ_{xx} being larger than the other components.

Fig. 11 shows the main view of computed stresses with time. It can be clearly seen that the stresses gradually concentrate to the fixed end in the first 0.5 seconds.

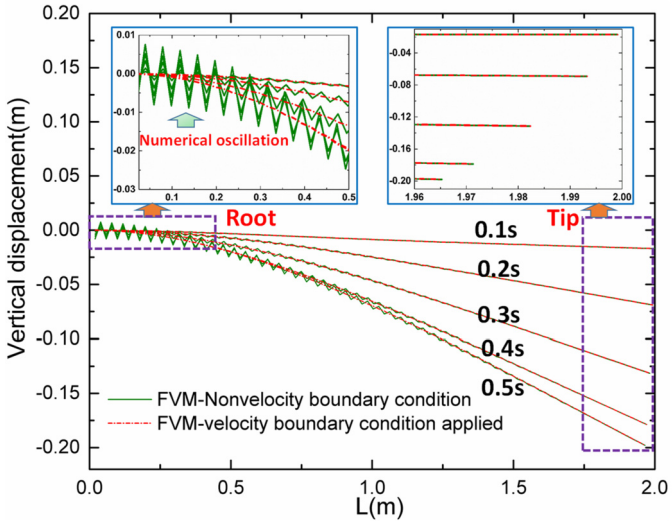

Fig. 9. Comparison of vertical displacement along the axis with different boundary conditions in 0-0.5 s.

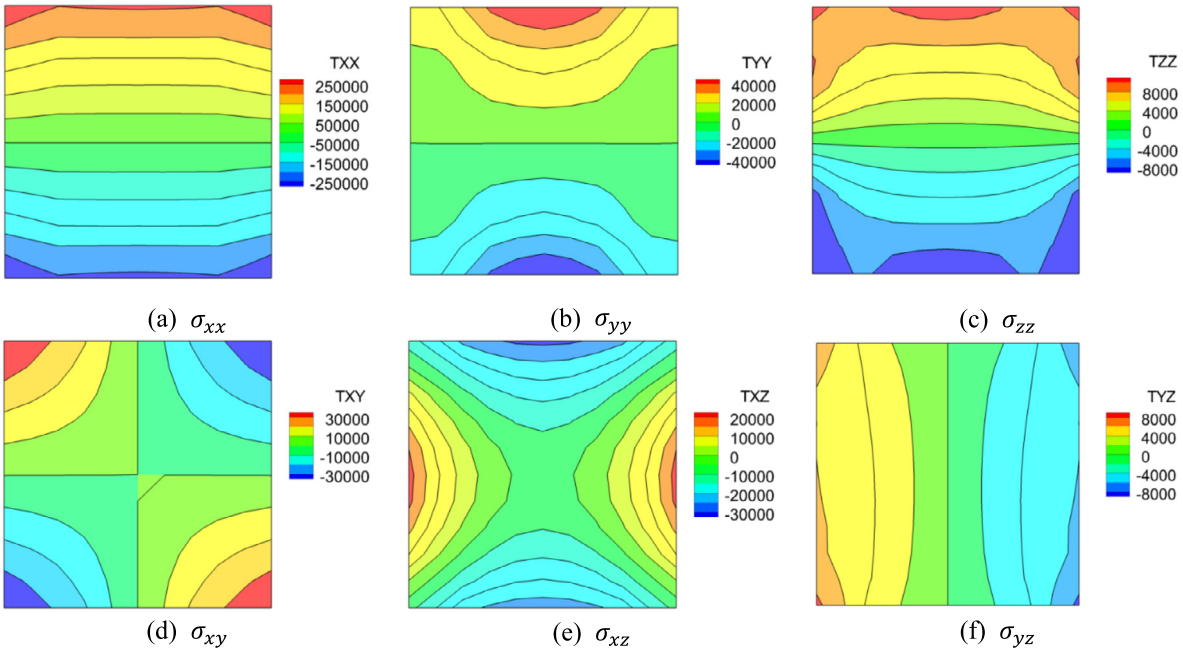

Fig. 10. Side view of the computed stresses at $t = 0.5$ (s) (Grid6: $20 \times 20 \times 200$) (Values are in Pa).

Table 4
Comparison of computational efficiency of different time steps.

Real time step size(s)	CFL_{max}	Iteration steps per pseudo time	Total steps per 0.005 s
0.005	4	3648	3648
0.001	18	87	435
0.0005	35	40	400
0.0002	60	8	200
0.0001	30	7	350
0.00005	15	6	600

2.2. Analysis of time step on accuracy and convergence

The effect of the time step on the accuracy is shown in Fig. 12, and the convergence plots for different real time steps at each pseudo time are shown in Fig. 13. It can be observed that the smaller time step not only improves the prediction accuracy of the amplitude but also affects the calculation efficiency. The FVM will converge quickly with a smaller time step, but will need to run for more time steps to simulate the same duration of real time. Table 4 counts the total number of iteration steps when the pseudo time step converges to 10^{-8} and cover 0.005 s. It can be observed that when $\Delta t = 0.0002$ s (1/500T, where T is the natural period of the cantilever), it only takes 200 steps to complete the operation, and the CFL_{max} can be 60.

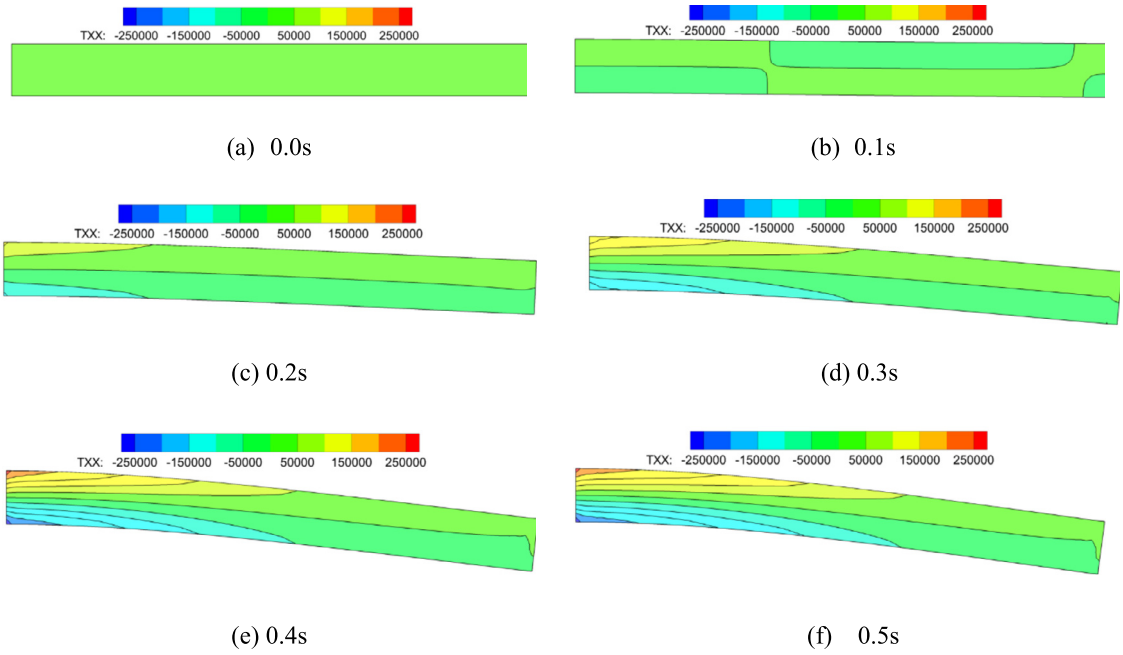

Fig. 11. Main view of the computed stress contours and variety with time (Grid6: $20 \times 20 \times 200$) (Values are in Pa).

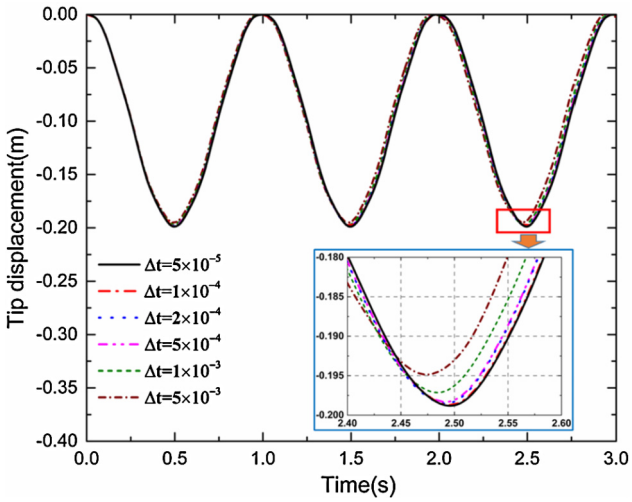

Fig. 12. Time step study for the 3D cantilever of grid 5 ($10 \times 10 \times 100$).

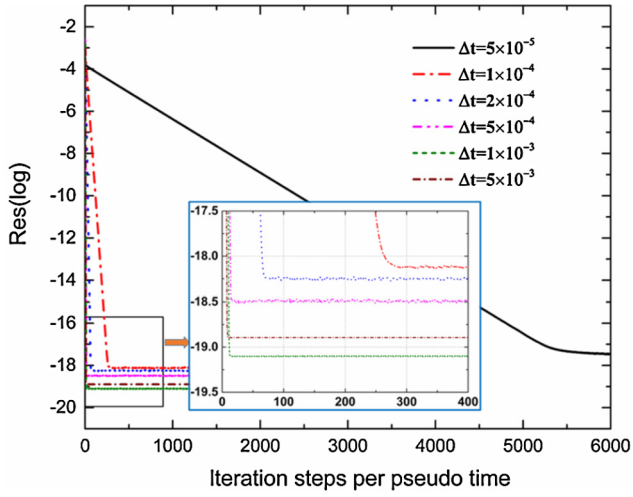

Fig. 13. Convergence plots with different time steps.

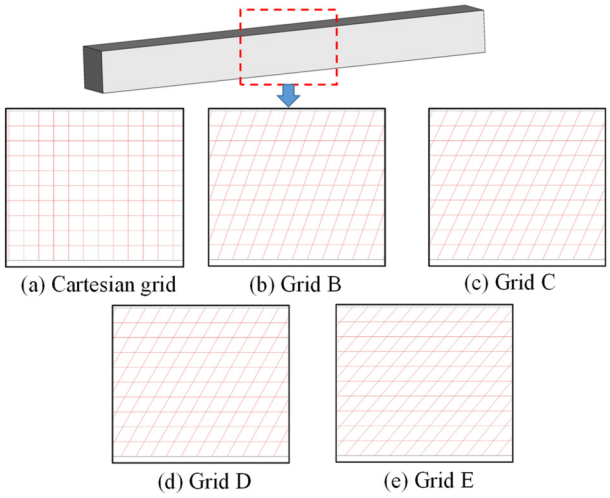

Fig. 14. General non orthogonal grid diagram.

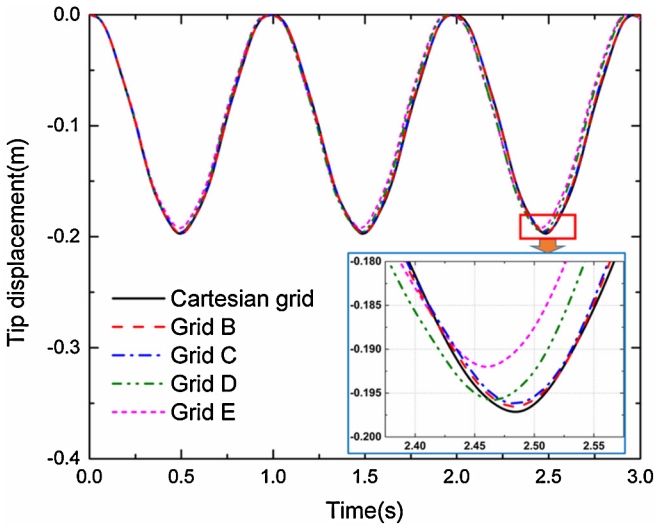

Fig. 15. Hexahedron grid study for the 3D cantilever.

2.3. Analysis of grid orthogonality on accuracy and convergence

To study the influence of grid orthogonality on the calculation accuracy of the FVM, the following six grids were used for analysis. These are shown in Fig. 14, where (a) is Cartesian grid, while the orthogonality of grids B-E is reduced.

The physical time step was set to 1×10^{-3} seconds, and the CFL was set to 10. The effect of the grid quality is shown in Fig. 15. The results show that the grid with high orthogonality can achieve higher accuracy, and the amplitude error of grid E is about 4%. Fig. 16 shows the residual convergence plots, and suggests that orthogonality can slightly improve the convergence speed. Generally speaking, good grid quality can effectively improve both the accuracy and efficiency. For application in helicopter blades or wings with complex shape, the multi block grid method can be used to improve mesh quality.

2.4. Application of multi block grid

Multi-block grids have been studied in this section. The computational domain is divided into four blocks (see Fig. 19), but the total number of cells in the computational domain remains unchanged. Information transfer between blocks is carried out through ghost cells. In addition, the MPI parallel library is used to improve the computational efficiency. It can be seen from Fig. 17 and Fig. 18 that compared with the single block grid, the multi-block method can also capture the amplitude and phase with high accuracy, and the computing efficiency can be improved nearly four times when computed in parallel.

Fig. 19 shows the vertical displacement contours of the single block and multi-block (4 blocks) grid. The displacement gradient does not change obviously at the interface between blocks. The results suggest that the block interface data exchange is successful. The results indicate that multiblock grid does have a slight effect on convergence and accuracy.

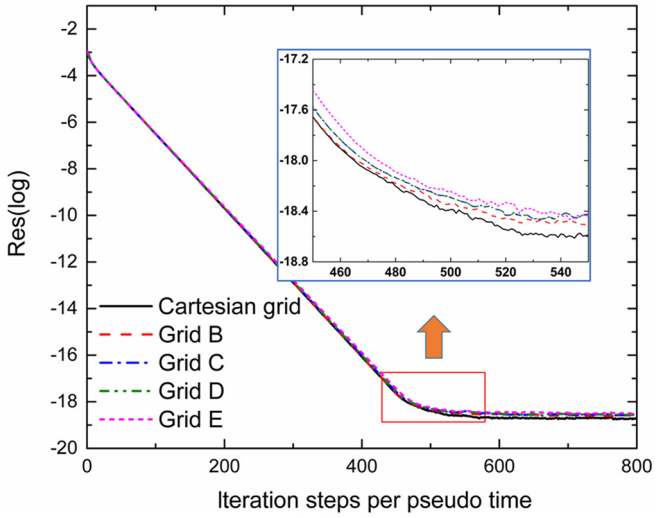

Fig. 16. Convergence plots with general non orthogonal grids.

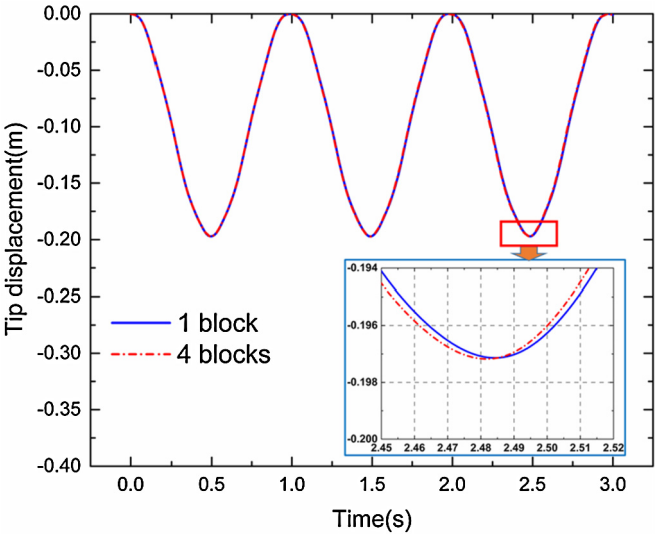

Fig. 17. Multi block grid study for the 3D cantilever.

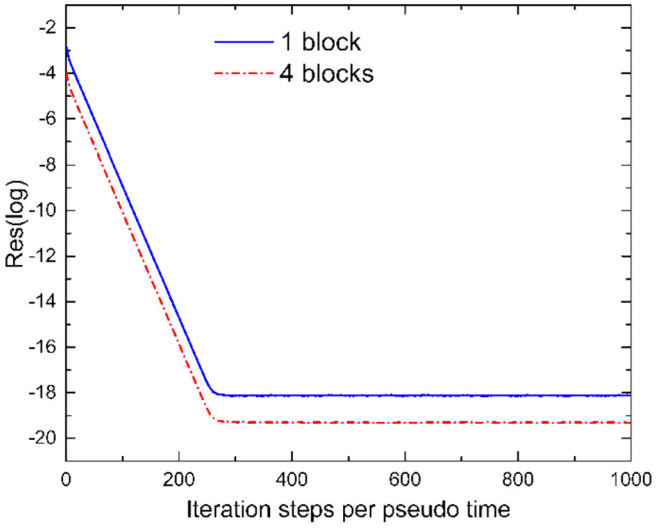

Fig. 18. Convergence plots with multi block grid.

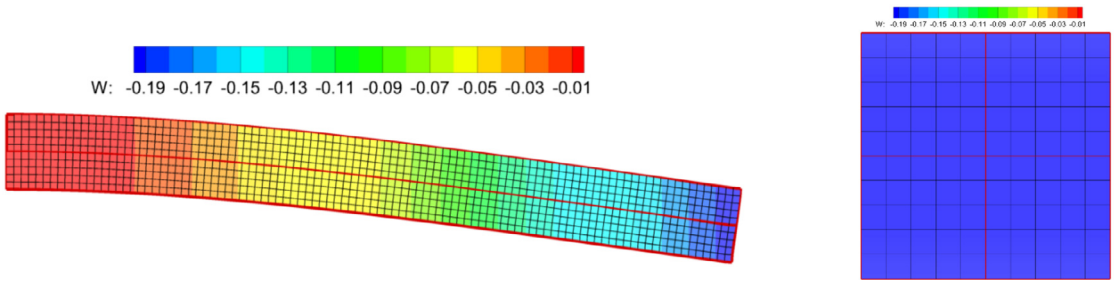

(a) Main view (b) Side view

Fig. 19. Vertical displacement contours of multi-block (4 blocks) grid (Values are in m).

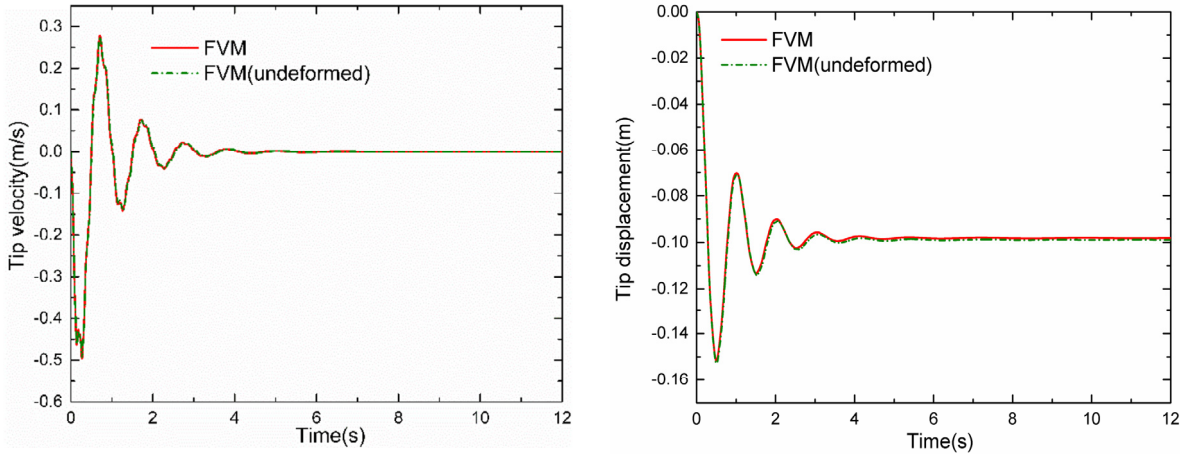

(a) Velocity (b) Displacement

Fig. 20. Response due to distributed pressure with 1.5% damping ratio.

2.5. Analysis of static state solution of cantilever

The static state solution was obtained by underdamped response of the cantilever using the proposed FVM. The static solution for this type of problem is determined analytically to be

$$y_{\max} = \frac{PL^4}{8EI_z} \tag{23}$$

The applied uniform pressure was 510.0 Pa which would result in a maximum static deflection of 0.1 m at the free end of the beam. The influence of grid deformation on the results is studied in this section. The forced vibration of the cantilever under constant load F can be described as the following:

$$\mathrm{y}(\mathrm{t}) = \left(\mathrm{y}_0 - \frac{F}{k}\right) \mathrm{e}^{-\zeta\omega_n t} \cos\omega_d t + \left[\frac{\zeta\omega_n \left(\mathrm{y}_0 - \frac{F}{k}\right) + \dot{\mathrm{y}}_0}{\omega_n\sqrt{1-\zeta^2}}\right] \mathrm{e}^{-\zeta\omega_n t} \sin\omega_d t - \frac{F}{k} \tag{24}$$

ω_n and ω_d are undamped and damped natural frequencies of the cantilever. $\zeta = \frac{C}{2\sqrt{km}}$ is critical damping ratio, which represents damping in the structure. $k = \frac{3EI}{l^3}$ is the stiffness of the structure [24][45]. Then the Eq. (1) could be written as:

$$\frac{\partial(\rho \boldsymbol{V})}{\partial t} - \nabla \cdot \boldsymbol{\sigma} + 2\varsigma\sqrt{k\rho}\frac{\partial \boldsymbol{U}}{\partial t} = \rho \boldsymbol{f} \tag{25}$$

Then the underdamped response of the cantilever with 1.5% damping ratio is also calculated. Fig. 20 shows the underdamped response of the cantilever. The simulation converges to 0.0989 maximum deflection with about -1.1% deviation at the free end of the deformed beam, and -0.9% deviation for the undeformed beam. The results show that the undeformed beam model is closer to the analytical solution, and this may be related to the mesh quality after the deformation process.

Fig. 21 shows the displacement contours of the static solution, the left plots are for the undeformed beam, and the right for the deformed beam. It can be observed that the deformed beam has little effect on the lagging and vertical displacement. However, the axial displacement is changed significantly.

Fig. 22 shows the axial displacement contours by FEM. Compared with Fig. 21(e) and (f), the maximum error of the surface axial displacement of the deformed beam is large, and the result of FVM is only about half of the FEM. The reason is that the FE model is based on the large deformation theory, while the linear elastic model with small deformation is applied in this paper.

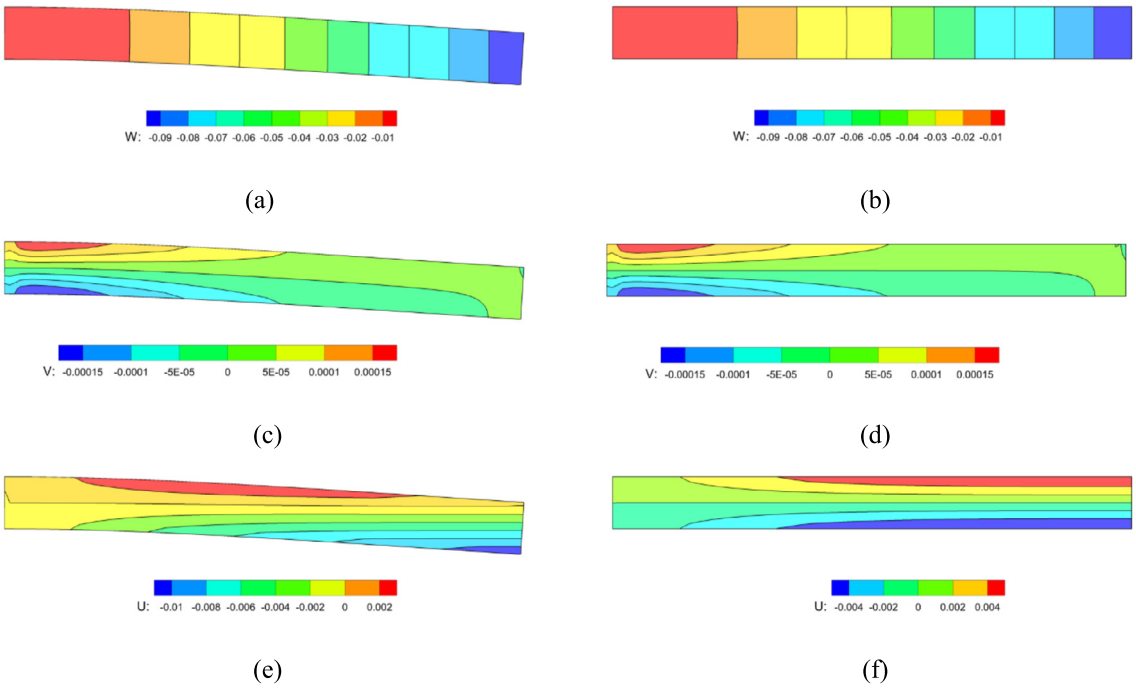

Fig. 21. Comparison of displacement contours with 1.5% damping ratio by FVM.

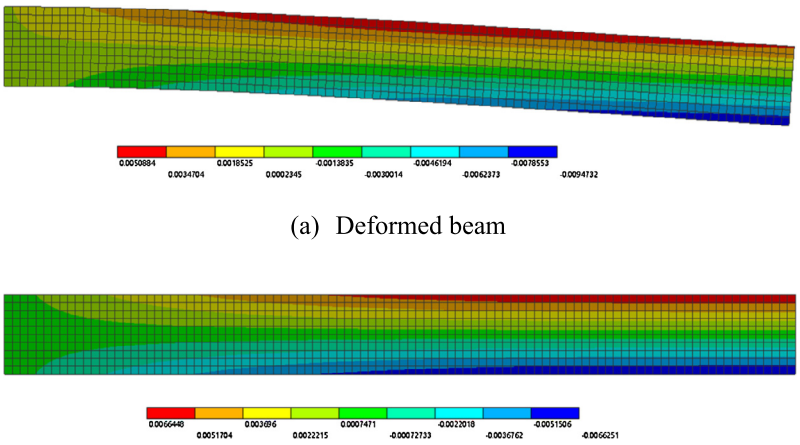

Fig. 22. Comparison of axial displacement contours with 1.5% damping ratio obtains by the FEM.

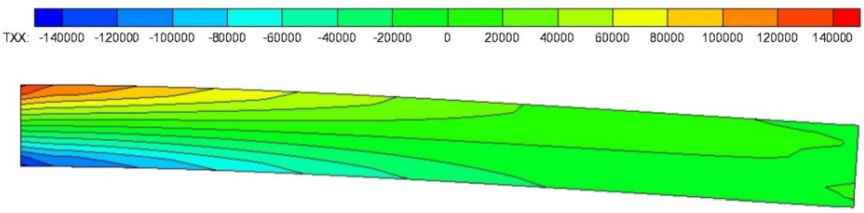

Fig. 23. Computed stress contours of the stability state (Values are in Pa).

The maximum bending stress at the root of the cantilever occurs at the upper surface [46], which is calculated as

$$(\sigma_{xx})_{\max} = \frac{My}{I_z} = \frac{3Pl^2}{h^2} \tag{26}$$

With the 510 Pa load, the maximum bending stress at the root of the cantilever is 153,000 Pa. The distribution of σ_{xx} obtained on grid 5 is presented in Fig. 23. The stress on the upper surface at the root of cantilever registers a value of 152,100 Pa, with about 0.5% deviation from the analytical results of 153,000 Pa.

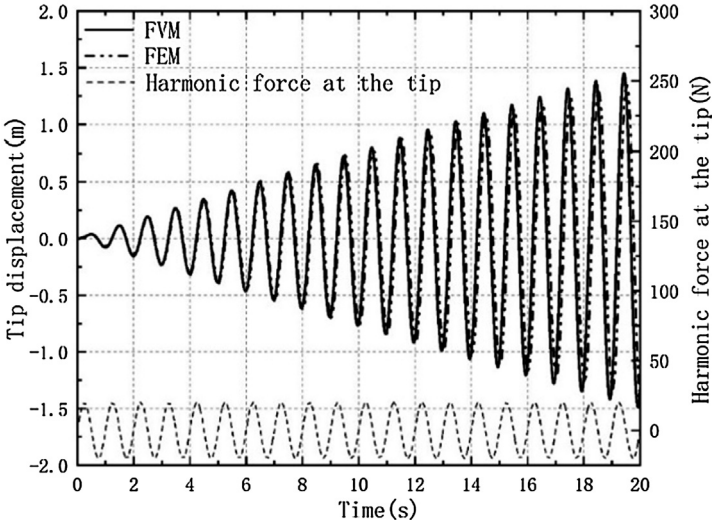

Fig. 24. Response due to a sinusoidal force input $F = 20\sin(2\pi t)$.

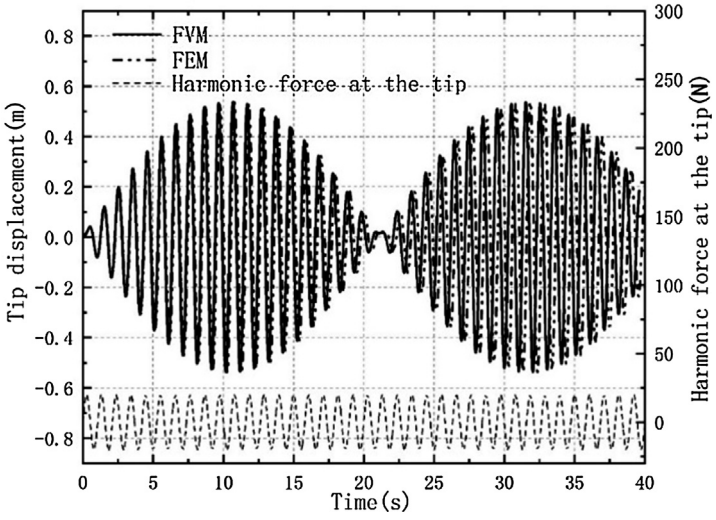

Fig. 25. Response due to a sinusoidal force input $F = 20\sin(1.9\pi t)$.

2.6. Verification of dynamic response of cantilever under harmonic excitation

To investigate the response accuracy of FVM under harmonic forcing, we replaced the distributed force with a concentrated force on the tip. The beam grid is composed of multi-block grids. The grid size is $10 \times 10 \times 100$. Fig. 24 shows the flexural deformation of the tip due to a sinusoidal force input $F = 20\sin(2\pi t)$, where 1 Hz is equal to the natural frequency of the beam. As anticipated, resonance occurs as shown in the solutions.

Fig. 25 shows a beating phenomenon when the forcing frequency of the previously applied load is 0.95 Hz. In both cases, the FVM solution was in perfect agreement with the FEM.

Fig. 26 shows the flexural deformation of the beam tip under the same load in conditions but for a forcing frequency of 50 Hz, and time step set to 10^{-5} s. The developed FVM method can accurately capture the high-order harmonic loads.

2.7. Analysis of a cantilevered beam with NACA0012 airfoil cross-section

To verify that the method can be applied to structures with complex shapes, the dynamic characteristics of a cantilever beam of NACA0012 cross-section are calculated and analyzed. Table 5 list the dimensions and material parameters of the beam.

As shown in Fig. 27(a), since there is no thickness at the trailing edge of the airfoil simulated, to prevent abnormal deformation of the trailing edge, we linearly reduce the applied constant load from the leading edge to the trailing edge of the airfoil to 0 Pa at 0.9C, where C is the chord length. The time step is taken as 0.001 s. The finite element method and the finite volume method developed were used to analyze the calculation results. The finite element results are calculated by ANSYS software. The multi-block grid is applied to generate the FVM grid, which is shown in Fig. 27(b). It can be seen that multi-block grid can greatly improve the quality of the grid inside the cantilever. The cell count is 180000.

Fig. 28 shows the dynamic tip response of the leading edge. The harmonic vibrations of the cantilever beam are captured by both methods. The amplitude and phase predictions of the two methods are basically consistent. This further proves that the current method can be applied to the solid dynamic analyses of general hexahedral multi-block grids.

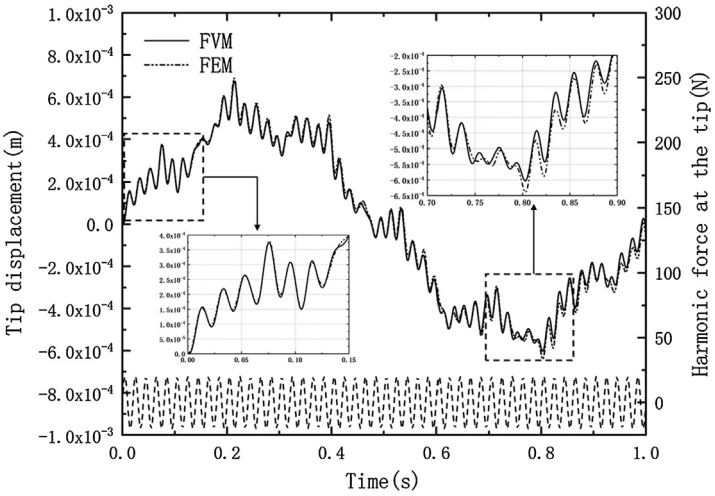

Fig. 26. Response due to a sinusoidal force input $F = 20\sin(100\pi t)$.

Table 5
Cantilever dimensions and material properties.

Property	Value
Cantilever length	3 m
Chord length	1 m
Density	2600 Kg m^{-3}
Young's modulus	10 MPa
Poisson's	0.3

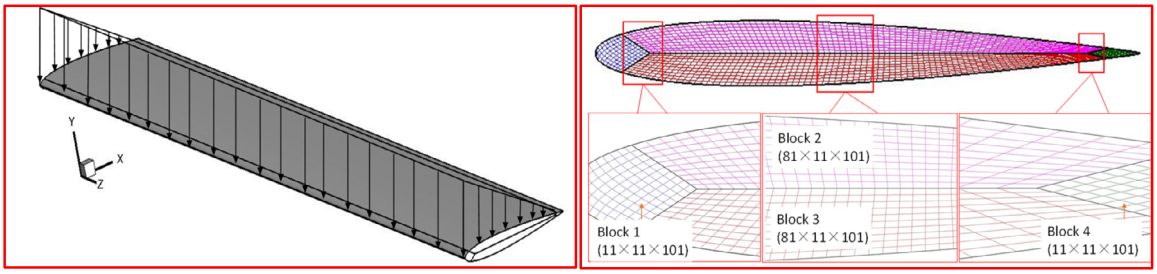

(a) (b)

Fig. 27. FVM mesh and cantilever beam subjected to a linear force along the chord.

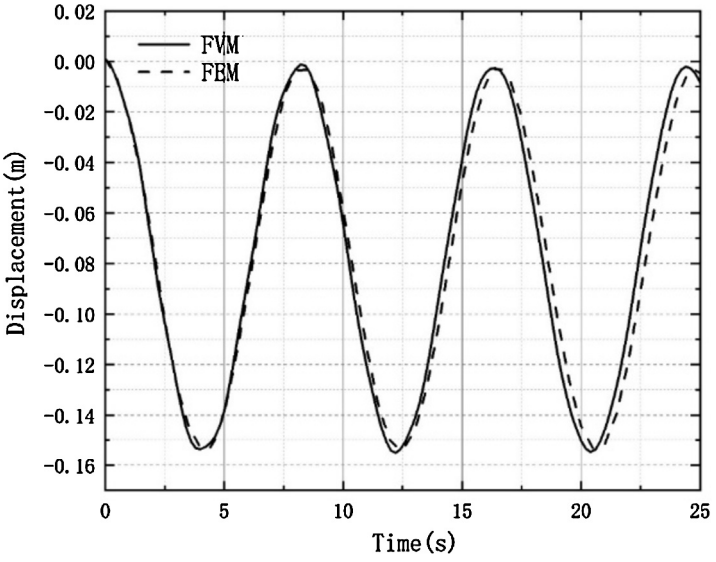

Fig. 28. Dynamic response of the cantilevered beam with NACA0012 airfoil.

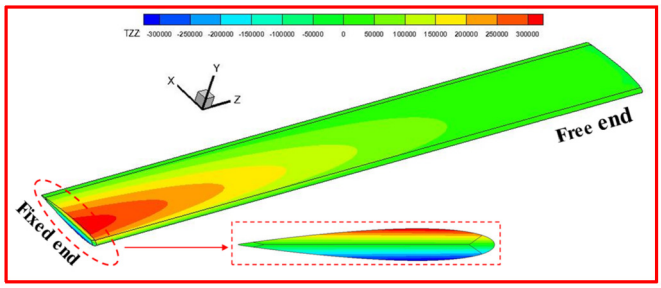

Fig. 29. 3D view of the computed stress contours (σ_{zz}) at $t = 3$ s (Values are in Pa).

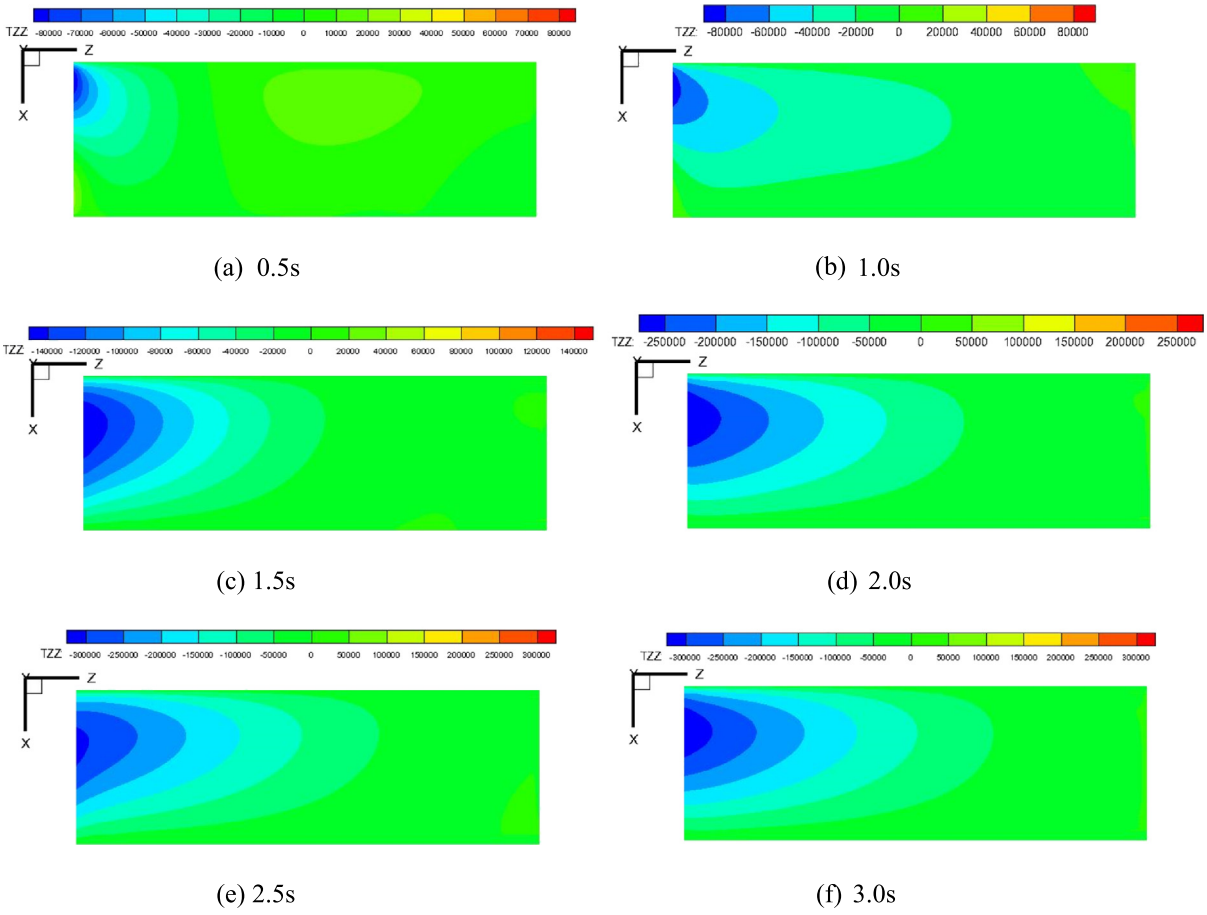

Fig. 30. Computed stress contours (σ_{zz}) and variety with time on the lower surface of the cantilever (Values are in Pa).

Fig. 29 is a three-dimensional plot of the normal stress (σ_{zz}) distribution of the cantilever beam. The stress is mainly concentrated on the upper and lower surfaces of the fixed end.

Figs. 30 and 31 show the displacement and stress contours of the lower surface of the cantilever beam in the first three seconds. The chord direction of the cantilever will be deformed when the Young's modulus of the material is small, resulting in changes in the shape the airfoil.

3. Conclusion and further work

A 3D cell-centred structured, multi-block finite volume method is proposed in this work for static and dynamic analyses of solids. Stresses are evaluated using Green's theorem based on grid cells. To obtain time accurate dynamic solutions, the implicit dual time-stepping scheme is employed. Local time-stepping, and residual smoothing in pseudo time are implemented to improve convergence. Numerical experiments prove that the method is accurate and efficient in the analysis of structural deformation and dynamics.

(1) The calculation error of FVM is large when the grid size is coarse. The accuracy of FVM could be improved significantly by increasing the grid size and reach as the same level as FEM. In the example of a 3D cantilever beam tested in this paper, the maximum error of static displacement was −0.9%, the maximum error of dynamic displacement was −1.29%, and the phase error was −0.64%. Resonance and beating phenomenon were clearly observed and correct pressure distributions were obtained in comparison to analytical results. The proposed numerical algorithm provides a good balance between accuracy and speed of computation.

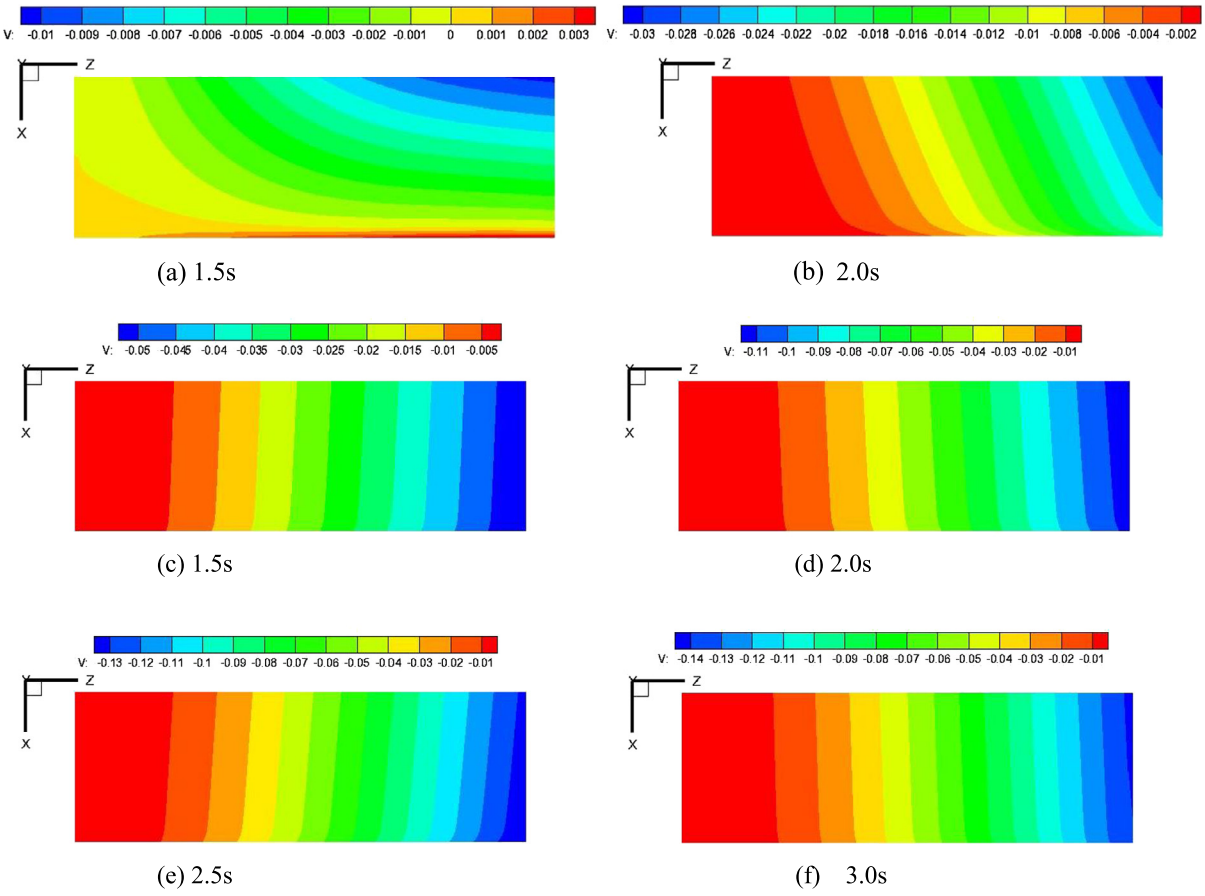

(a) 1.5s (b) 2.0s

(c) 1.5s (d) 2.0s

(e) 2.5s (f) 3.0s

Fig. 31. Computed displacement contours (v) with time on the lower surface of the cantilever.

(2) The smaller time step not only improves the prediction accuracy of the amplitude but also affects the calculation efficiency. When $\Delta t = 0.002$ s (1/500T, where T is the natural period of the cantilever), it only takes 200 steps to complete the operation, and the $\mathrm{CFL}_{\max}$ can be 60. Besides, good grid quality can effectively improve the accuracy and efficiency.

(3) This method can be applied to the general hexahedral grids, and good grid quality can achieve the same accuracy as a Cartesian grid. The developed multi-block, finite volume method is suitable for use with the numerical discretization schemes used in the CFD solver, allowing efficient CFD/CSD coupling with no data interpolations. In the future applications of the method to aeroelastic problems is planned and will be reported separately.

Declaration of competing interest

The authors declare that they have no known competing financial interests or personal relationships that could have appeared to influence the work reported in this paper.

Acknowledgement

This research is supported by the National Natural Science Foundation of China (12032012), Engineering and Physical Sciences Research Council of UK. Besides, this research is a project funded by the Priority Academic Program Development of Jiangsu Higher Education Institutions (PAPD). The financial support of the Engineering and Physical Sciences Research Council (EPSRC) of the UK is gratefully acknowledged (EP/S013814/1).

References

[1] T. Guo, E. Shen, Z. Lu, D. Zhou, J. Wu, Thermal flutter prediction at trajectory points of a hypersonic vehicle based on aerothermal synchronization algorithm, Aerosp. Sci. Technol. 94 (2019) 105381.
[2] Y. You, D. Na, S.N. Jung, Improved rotor aeromechanics predictions using a fluid structure interaction approach, Aerosp. Sci. Technol. 73 (2017) 118–128.
[3] N. Vidanovi, B. Rauo, G. Kastratovi, et al., Aerodynamic-structural missile fin optimization, Aerosp. Sci. Technol. 65 (2017) 26–45.
[4] A. Naseri, A. Totounferoush, Ignacio González, et al., A scalable framework for the partitioned solution of fluid-structure interaction problems, Comput. Mech. 66 (2020) 471–489.
[5] A. Jendoubi, A fast mesh deformation method for fluid-structure interaction problems, IOP Conf. Ser., Mater. Sci. Eng. 715 (2020) 12–16.
[6] E. Lefran Ois, A simple mesh deformation technique for fluid-structure interaction based on a submesh approach, Int. J. Numer. Methods Eng. 75 (2010) 1085–1101.
[7] S.R. Idelsohn, E. Oñate, Finite volumes and finite elements: two 'good friends', Int. J. Numer. Methods Eng. 37 (2010) 3323–3341.
[8] M.V. Jr, P.A. Munoz-Rojas, G. Filippini, On the accuracy of nodal stress computation in plane elasticity using finite volumes and finite elements, Comput. Struct. 87 (2009) 1044–1057.
[9] I. Demirdi, D. Martinovi, Finite volume method for thermo-elasto-plastic stress analysis, Comput. Methods Appl. Mech. Eng. 109 (1993) 331–349.

[10] C.J. Greenshields, H.G. Weller, A. Ivankovic, The finite volume method for coupled fluid flow and stress analysis, Comput. Model. Simul. Eng. 4 (1999) 213–218.
[11] K. Zarrabi, A. Basu, A finite volume element formulation for solution of elastic axisymmetric pressurized components, Int. J. Press. Vessels Piping 77 (2000) 479–484.
[12] A. Sato, I. Ohnaka, J. Iwane, Stress analysis by finite volume method for prediction of porosity and deformation defects of spheroidal graphite castings, J. Jpn. Foundry Eng. Soc. 78 (2006) 231–237 (in Japanese).
[13] N. Fallah, A method for calculation of face gradients in two-dimensional cell centred finite volume formulation for stress analysis in solid problems, Sci. Iran. 15 (2008) 286–294.
[14] J.D. Bressan, M.M. Martins, M. Vaz Jr, Stress evolution and thermal shock computation using the finite volume method, J. Therm. Stresses 33 (2010) 533–558.
[15] S. Das, S.R. Mathur, J.Y. Murthy, An unstructured finite-volume method for structure electrostatic interactions in MEMS, Numer. Heat Transf., Part B, Fundam. 60 (2011) 425–451.
[16] I. Demirdi, A fourth-order finite volume method for structural analysis, Appl. Math. Model. 40 (2016) 3104–3114.
[17] M.M. Martins, J.D. Bressan, S.T. Button, Finite volume analysis with the MacCormack method applied to metal flow in forward extrusion, Univers. J. Mech. Eng. 5 (2017) 1–8.
[18] A. Amraei, N. Fallah, A cell-centred finite volume formulation for the calculation of stress intensity factors in Mindlin-Reissner cracked plates, Civ. Eng. J. 3 (2018) 1366–1385.
[19] N. Fallah, M. Delzendeh, Free vibration analysis of laminated composite plates using meshless finite volume method, Eng. Anal. Bound. Elem. 88 (2018) 132–144.
[20] N. Fallah, A. Ghanbary, A displacement finite volume formulation for the static and dynamic analysis of shear deformable curved beams, Sci. Iran. 25 (2018) 999–1014.
[21] O.I. Hassan, A. Ghavamian, C.H. Lee, et al., An upwind vertex centred finite volume algorithm for nearly and truly incompressible explicit fast solid dynamic applications: total and updated Lagrangian formulations, J. Comput. Phys. 9 (2019) 852–861.
[22] P. Cardiff, I. Demirdzic, Thirty years of the finite volume method for solid mechanics, preprint, arXiv:1810.02105, 2018.
[23] X. Lv, Y. Zhao, X.Y. Huang, G.H. Xia, X.H. Su, A matrix-free implicit unstructured multi grid finite volume method for simulating structural dynamics and fluid-structure interaction, J. Comput. Phys. 225 (2007) 120–144.
[24] G.H. Xia, Y. Zhao, J.H. Yeo, X. Lv, A 3D implicit unstructured-grid finite volume method for structural dynamics, Comput. Mech. 40 (2007) 299–312.
[25] G.H. Xia, C.l. Lin, An unstructured finite volume approach for structural dynamics in response to fluid motions, Comput. Struct. 86 (2008) 684–701.
[26] S.R. Sabbagh-Yazdi, M.T. Alkhamis, N.E. Mastorakis, M. Esmaili, Finite volume analysis of two-dimensional strain in a thick pipe with internal fluid pressure, Int. J. Math. Models Methods Appl. Sci. 2 (2008) 162–167.
[27] N. Mastorakis, S.R. Sabbagh-Yazdi, M.T. Alkhamis, Explicit 2D matrix free Galerkin finite volume solution of plane strain structural problems on triangular meshes, Int. J. Math. Comput. Simul. 1 (2008) 1–8.
[28] S.R.S. Yazdi, T.A.S. Abadi, Sequential computations of two-dimensional temperature profiles and thermal stresses on an unstructured triangular mesh by GFVM method, Internat. J. Civ. Eng. 9 (2011) 171–182.
[29] S.R. Sabbagh-Yazdi, M. Esmaili, M.T. Alkhamis, Symmetric conditions for strain analysis in a long thick cylinder under internal pressure using NASIR unstructured GFVM solver, Jordan J. Civ. Eng. 5 (2011) 258–267.
[30] W. Chen, Y. Yu, An unstructured finite volume method for impact dynamics of a thin plate, J. Mar. Sci. Appl. 11 (2012) 478–485.
[31] M. Zhu, P. Ming, L. Xuan, et al., An unstructured finite volume time domain method for structural dynamics, Appl. Math. Model. 36 (2012) 183–192.
[32] Y.Y. Tsui, Y.C. Huang, C.L. Huang, S.W. Lin, A finite-volume-based approach for dynamic fluid-structure interaction, Numer. Heat Transf., Part B, Fundam. 64 (2013) 326–349.
[33] R. Suliman, O.F. Oxtoby, A.G. Malan, et al., An enhanced finite volume method to model 2D linear elastic structures, Appl. Math. Model. 38 (2014) 2265–2279.
[34] P. Alagappan, K.R. Rajagopal, A.R. Srinivasa, Wave propagation due to impact through layered polymer composites, Compos. Struct. 115 (2014) 1–11.
[35] P. Alagappan, K.R. Rajagopal, A.R. Srinivasa, A three dimensional finite deformation viscoelastic model for a layered polymeric material subject to blast, Compos. Struct. 159 (2017) 382–389.
[36] K. Hejranfar, M.H. Azampour, Assessment of cell-centered and cell-vertex finite volume approaches for computation of 2D structural dynamics on arbitrary quadrilateral grids, Comput. Model. Eng. Sci. 106 (2015) 395–439.
[37] M.M. Selim, R. Koomullil, D.R. Mcdaniel, Finite volume based fluid-structure interaction solver, in: 58th AIAA/ASCE/AHS/ASC Structures, Structural Dynamics, and Materials Conference, 2017.
[38] P. Grete, F.W. Glines, B.W. Oshea, K-Athena: a performance portable structured grid finite volume magneto hydro dynamics code, IEEE Trans. Parallel Distrib. Syst. (2020) 1.
[39] A. Gross, H.F. Fasel, Multi-block Poisson grid generator for cascade simulations, Math. Comput. Simul. 79 (2008) 416–428.
[40] H. Ishizaki, I. Ishikawa, High parallelization efficiency in barotropic-mode computation of ocean models based on multi-grid boundary ghost area, Ocean Model. 13 (2006) 238–254.
[41] S. Das, S.R. Mathur, J.Y. Murthy, An unstructured finite-volume method for structure-electrostatics interactions in MEMS, Numer. Heat. Transf., Part B, Fundam. Int. J. Comput. Methodol. 60 (2011) 425–451.
[42] S. Das, Fluid-structure interactions in microstructures, PhD thesis, The University of Texas at Austin, 2013.
[43] Y.H. Tseng, J.H. Ferziger, A ghost-cell immersed boundary method for flow in complex geometry, J. Comput. Phys. 192 (2003) 593–623.
[44] M.M. Selim, M. Mohamed, R.P. Koomullil, D.R. Mcdaniel, Linear elasticity finite volume based structural dynamics solver, in: AIAA Modeling and Simulation Technologies Conference, 2016.
[45] GaryC Hart, Structural Dynamics for Structural Engineers, John Wiley & Sons, Inc., 2000.
[46] S.P. Timoshenko, J.N. Goodier, Theory of Elasticity, McGraw-Hill, 1982.